Thesis Title

A subtitle of your thesis

Author name

Thesis submitted for the degree of
Master in Master's Program Name <change at
main.tex>
60 credits

Department Name <change at main.tex>
Faculty name <change in duoforside.tex>

UNIVERSITY OF OSLO

Spring 2022

Thesis Title

A subtitle of your thesis

Author name

Abstract

Contents

List of Figures

List of Tables

Preface

Chapter 1

Introduction

some introduction on the importance of discovering new materials and alloying.
Need something on thermoelectricity related to both the band gap and high-entropy alloys.

High-entropy alloys is a novel class of materials based on alloying multiple components, as opposed to the more traditional binary alloys. This results in an unprecedented opportunity for discovery of new materials with a superior degree of tuning for specific properties and applications. Recent research on high-entropy alloys have resulted in materials with exceedingly strong mechanical properties such as strength, corrosion and temperature resistance, etc **find references**. Meanwhile, the functional properties of high-entropy alloys is vastly unexplored. In this study, we attempt to broaden the knowledge of this field, the precise formulation of this thesis would be an exploration on the possibilities of semiconducting high-entropy alloys.

A key motivation of this thesis is the ability to perform such a broad study of complex materials in light of the advances in material informatics and computational methods. In this project, we will employ Ab initio methods backed by density functional theory on top-of the line supercomputers and software. 20 years ago, at the breaking point of these methods, this study would have been significantly narrower and less detailed firstly, but secondly would have totaled ... amount of CPU hours to complete (**Calculate this number**). In the addition to the development in computational power, is also the progress of modeling materials, specifically we will apply a method called Special Quasi-random Structures (SQS) to model high-entropy alloys or generally computationally complex structures. Together with the open landscape of high-entropy alloys described above, these factors produce a relevant study in the direction of applying modern computational methods to progress the research of a novel material class and point to promising directions for future research.

In specifics, this thesis revolve around the electrical properties of high-entropy alloys, mainly the band gap as this is the key indicator for a semiconducting material and it's applicability. Semiconductors are the building blocks in many different applications in today's world, ranging

from optical and electrical devices, to renewable energy sources such as solar and thermoelectricity. Given the economic and sustainable factors concerning silicon, in addition to its role in relevant applications such as microelectronics and solar power. Silicon emerges as a natural selection to build our alloys around. Furthermore, the development and research on both high entropy alloys and metal silcides have been heavily centered around 3d transition metals. Keeping in line with the economic and environmental factors, we will continue this direction by focusing on high entropy stabilized sustainable and economic 3d metal silicides **Not happy with this writing**. Throughout the study we will analyze a great number of permutations of 3d silicides, from different initial metal silicides such as $CrSi_2, FeSi_2, MnSi_{1.75}, Fe_2Si$, each with distinct properties relating to the band gap, crystal structure and metal to silicon ratio. In addition, the permutations include numerous metal distributions and elements within the 3d-group of metals. Examples are Co, Cr, Fe, Mn, and Ni.

Given a background in high-entropy alloys, one could ask if this study is truly sensible. In the later sections we will cover the details of this field, and it quickly become clear that the materials investigated in this study does not fall under the precise definition of high-entropy alloys, nor do we intend to explore the properties and factors relating to high-entropy stabilized alloys such as the configurational entropy, phase stability and finite temperature studies. However this study is motivated from the discovery of these materials and promising properties, and venture into a more hypothetical space of materials, enabled by the computational methods available to study the potential properties of such materials. On the other hand, very recent studies **Mari, and other HEA silicide study** have experimentally synthesized high-entropy disilicides, thus in some way justifying the direction of this project.

We begin this project by reviewing key concepts of solid-state physics for readers lacking a background in materials science, and an introduction to the base 3d silicides of the experimental work. Later follows a theoretic walk-through of the relevant concepts of this thesis, these topics include high-entropy alloys, special quasi-random structures, and density functional theory. Next we shine light on the implementation of DFT in this project, and other computational details required to reproduce the results in this thesis, such as the use of the Vienna Ab Initio Simulation Package (VASP) and implementation of SQS. Finally we present the results of our study, these include the band gap and electronic properties of various structures and the success and challenges of the computational methods applied throughout the study.

Part I

Theory

Part II

Methodology and Implementation

Part III

Results and Discussion

Change this introduction to fit the final product! In this one year long project, we have collected results of a great number of materials with various structures and compositions. The initial experimentation was based on high-entropy silicides of the Fe_2Si unit cell, created from the special quasi-random structure approach as described above. Despite the non-semiconducting character of this compound, we worked under the idea that the extraordinary properties that have been observed in high-entropy alloys through effects such as the cocktail effect, we could discover specific combinations of elements that would yield a semiconductor. In addition, the ratio between silicon atoms to metals allowed us to create nearly eqvimolar high-entropy alloys.

Following this attempt, we transitioned into studying high-entropy silicides based on well known semiconducting 3d silicides such as $\beta-FeSi_2$, $CrSi_2$ and $MnSi_{1.75}$. The main outcome of this project is that for all 4 different starting silicides, we could only produce high-entropy silicides from one unit cell, furthermore in this cell only one specific compositions of elements was semiconducting. This was $Cr_{0.25}Fe_{0.25}Mn_{0.25}Ni_{0.25})Si_2$, herein CFMN, in the $\beta-FeSi_2$ crystal structure.

This section will be structured in the following manner, firstly we will investigate the CFMN (fesi2) compound and various permutations of the composition. Thereafter we will look at other possible compositions of fesi2 based high-entropy silicides, and lastly test the CFMN composition in other crystal symmetries. In final we will present an overview of the complete study and the various compounds that have been investigated in order to propose promising directions and guideline future research directions in this field. In this way, we aim to understand the uniqe properties of CFMN (fesi2) and why this particular compound is semiconducting compared to the other testes structures in this project. Properties we will cover is the overall stability by total energy and corresponding enthalpy of formation, the magnetic properties and which elements contribute to the magnetism. But in majority, we will look at the band gap and related properties, as this is the main motivation and distinction of the study.

Chapter 7

$(CrFeMnNi)Si_2$ in the $\beta-FeSi_2$ structure

7.1 Bulk $\beta-$ $FeSi_2$

$\beta - FeSi_2$ in the orthorombic cmce crystal lattice is a well known semi-conductor with an experimentally measured band gap of around 0.85 ev at room temperature [1]. The nature of the band gap is under debate, all though most ab inito studies point to an indirect gap, experimental work result in a direct gap. In our study we find an indirect band gap of 0.65 eV with PBE, in comparison materials project find a band gap of 0.70 eV. This slight discrepancy is most likely down to use of different parameters in the calculations, for example the cutoff energy or number of k-points. In accordance with materials project we find that this compound is nonmagnetic. This can be seen from the electronic density of states in figure 7.1 by that the DOS and hence band gap is identical in both spins.
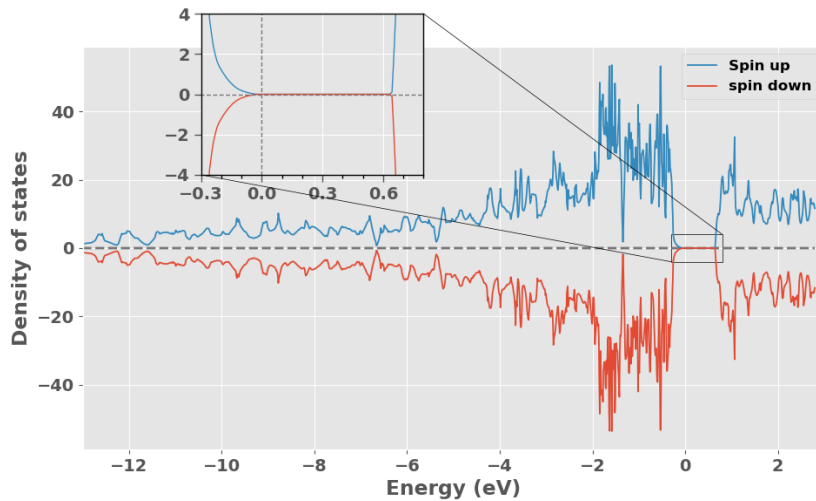
Figure 7.1: Density of states (PBE) $\beta-$ $FeSi_2$

We calculate the enthalpy of formation ΔH_f as the difference in total

energy between the product and sum of reactants. For the FeSi2 compound consisting of 16 iron atom sand 32 silicon we get $\Delta H_f = -327.72eV - (16 \cdot -8.32eV + 32 \cdot - -5.42eV = -21.16eV$, where the total energy per atom of iron and silicon was calculated separately for the respective base elements with identical parameters as used for the $FeSi_2$ calculation. Typically ΔH_f is listed in $kJmol^{-1}$, thus we get in final an enhalpy of formation $DeltaH_f = -42.552KjJmol^{-1}$. We note that this value is quite far away from other experimental results, such as $-74KJmol^{-1}$ in [2]. However this value correspond to the material at room temperature, while we have only looked at the ground state.

7.2 $(CrFeMnNi)Si_2$ SQSs

Details on both alloys and the bulk $FeSi_2$ structure is covered in section 6.2, the SQSs can be seen in figure 6.1. Below in table 7.1 we list the total energy per atom (Toten), final magnetic moment (Mag) and band gap (E_G) of the five distinct SQSs, plus the corresponding enthalpy of formation ΔH calculated from the mean total energy. For simplicity we denote the 5 supercells as A, B, C, D and E.

SQS	Toten (eV)	Mag (μ_B)	E_G (eV)
A	-6,6080	0.0833	0.0280
B	-6,6138	0.0833	0.0523
C	-6,6063	0.0834	0.0344
D	-6,6155	0.0833	0
E	-6,6089	0.0833	0.0495
Mean	-6.6105	0.0833	0.0328
Std	0.0039	0.0000	0.0210
ΔH	-11.5000 eV	-	-

Table 7.1: Total energy per atom, final magnetic moment and band gap of 5 unique SQS of $(CrFeMnNi)Si_2$ based on the $\beta- FeSi_2$ unit cell.

In addition to the mean energy we include the standard deviation "std" of the set to observe how far each supercell is from the mean value for different properties. Clearly both the total energy and magnetic moment show very little variation if any between SQSs which is expected seeing as the only difference is the atomic configuration. Contrary we observe greater variation in the band gap between SQSs, ranging from 0.02 - 0.05 eV, nevertheless much smaller than the the parent bulk material. On the other side we find that the magnetic moment has increased compared to in the bulk structure. Seen throughout all SQSs, the local magnetic moments is the largest for Cr followed by Mn, on the other hand the ferromagnetic elements Fe and Ni have small negative moments. This is an odd result, in calculations with identical parameters of the base

elements we find that Cr is non, Fe and ni is .., same with manganese. In HEAs specifically we saw in section 2.2 that in several cases particularly chromium reduce the magnetization of the compound. There are however several uncertainties concerning the listed magnetic values in this project, and the reported values are meant to be superficial indications of the magnetism in the real material. For example we have the limitations mentioned previously about both DFT and special quasi-random structures to model magnetic and particularly paramagnetic materials. The latter especially is as an important factor, as the outcome of the base elements are in much better agreement with other experimental data, such as materials project. This could be related to the SQSs distinct for this project, where we kept the Si sites in the lattice constant and restricted the 3d elements to occupy exclusively the Fe sites in the lattice. Such restrictions could impact the magnetic interactions between elements compared to in a real random alloy. Lastly each SQS have been tested solely with co-linear spin polarization, thus negleticng the many other possible configurations. The precise magnetic properties was compromised due to the large computational demand of locating the optimal magnetic configuration of each SQS and composition, and the focus of this project leaning more towards the band gap of the structures.

In terms of the total energy the most and least stable SQSs are "D" and "A" respectively. Based on the total energy between SQSs, D is then the most representative configuration of the real material. However most likely all five SQSs and other possible SQSs would appear as local orderings in domains of the real material with a certain probability. Therfore we will consider the results of the other SQSs as well as the most stable supercell. Furthermore the total energy alone is not sufficient to evaluate the stability. In this project we have not considered factors such as the confirational entropy or the optimized magnetic configuration of each structure. Additionally we have only studied the ground state and thus have no knowledge of the properties at finite temperatures. Hence the relationships and properties between the five SQSs listed in table 7.1 are not rigid.

7.2.1 The band gap

As seen in table 7.1, the band gap of the alloys are severely reduced from the bulk material, and show variation between each of the five SQSs. We observed a maximum band gap of 0.05 eV in SQS B, and on the flip side a 0 band gap in SQS D. The density of states of the respective structures can be seen below in fiugres 7.2 and 7.3.
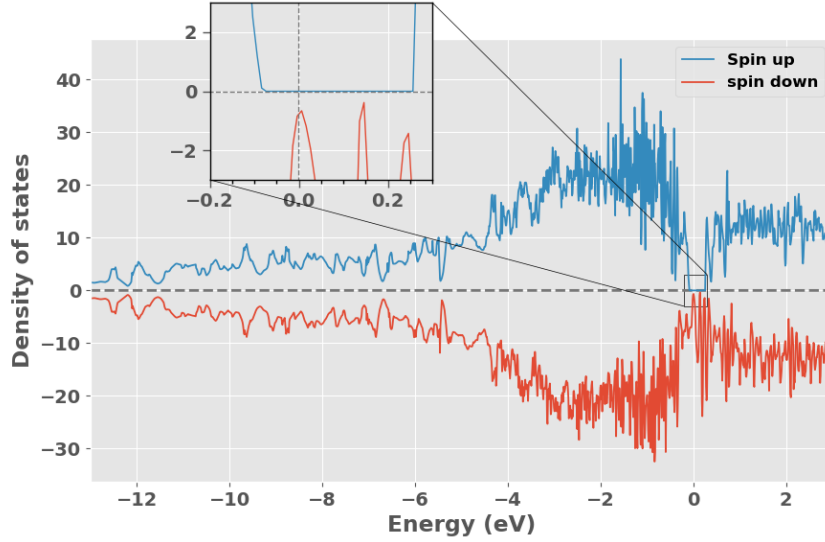
Figure 7.2: Density of states of SQS D (CrFeMnNi)Si$_2$ with PBE.
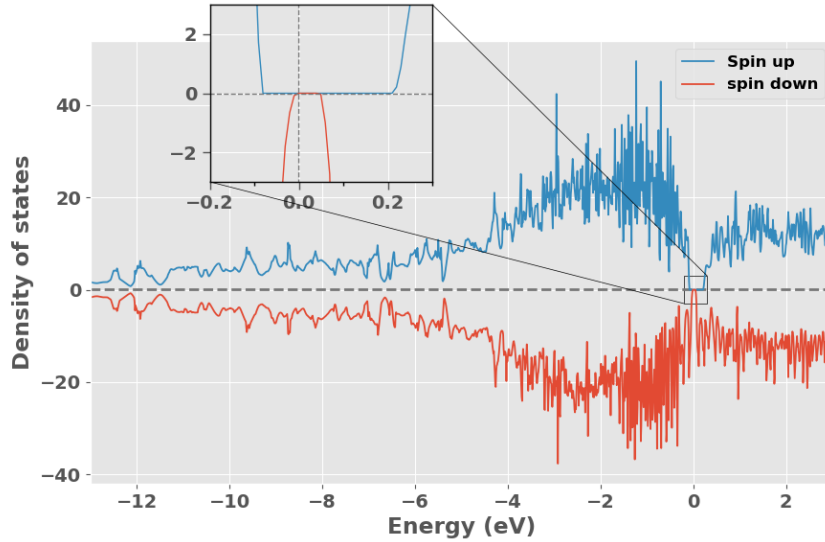
Figure 7.3: Density of states of SQS B (CrFeMnNi)Si$_2$ with PBE.

In figure 7.2 and 7.3 we observe that the band gap in both SQS D and B in accordance with the magnetic property is different between spins. Going

forward we will refer to the band gap in spin up as E_G^{up}, and spin down as E_G^{dw}. Clearly in both D and B $E_G^{\text{up}} > E_G^{\text{dw}}$ with no gap in spin down in D and 0.05 eV in B compared to around 0.3 eV in spin up in both structures. Comparing to the values listed in table 7.1 it's clear that the total band gaps of the respective structures correspond to the narrow or nonexistent band gap in spin down. To obtain further and more precise information on the band gap we look to the calculated Kohn-Sham eigenvalues, where the band gap can be calculated by subtracting the lowest energy unoccupied eigenstate in the conduction band to the highest energy occupied eigenstate in the valence band. The eigenvalue band gaps, denoted as E_G^{eigen} can be seen below in table 7.2 for all five SQS, the density of states of SQS A, C and E can be found in appendix [REF].

SQS	$E_G^{\text{up, eigen}}$ (meV)	$E_G^{\text{dw, eigen}}$ (meV)	$E_G^{\text{tot, eigen}}$ (meV)
A	81.4	52.2	28.1
B	293	52.2	52.2
C	236	34.3	34.3
D	339	0.00	0.00
E	308	50.0	50.0

Table 7.2: Band gap of the 5 SQSs of $(CrFeMnNi)Si_2$ calculated from the eigenvalues in spin up, down and total.

Alike the bulk material, these gaps are indirect. It would have been instructive to visualize and analyze the energy bands by plotting the band structure. Unfortunately this is neither simple to perform or interpret in large supercells consisting of several elements and a large number of energy bands. One solution is to do band-unfolding, but given the complex structure and implementation of the special quasi-random structures method in VASP this proved too challenging for the scope of this project.

A key point regarding the band structure of SQS D is the presence of what we will call defect states. In this structure the highest occupied conduction band is 128 for spin up states and band 124 in spin down, thus a difference of 4 bands between spins. For the spin down states we find that the highest energy valence band, ie 124 have states with occupancy both slightly bellow 1.00 and above at several k-points. Likewise the lowest energy conduction band (125) have partially filled states above 0.00 and bellow. The case of occupancy either above or bellow completely full or completely empty is simply a numerical inaccuracy well-known to calculations that apply the Tetrahedron method with Bloch corrections and have no real impact on the results. The second case where we have partially filled eigenstates in the conduction band and not completely filled states valence band is a familiar term in random alloys [3] in which the forbidden energy gap is contaminated by defect states. To further study

this effect we introduce $E_G^{\text{eigen}}(occ)$ to represent the band gap calculated at a occupancy cutoff occ in the eigenvalues. Such that $E_G^{\text{up, eigen}}(0.99)$ is the band gap in spin calculated from the eigenvalues with occupancy above 0.99. Equivalently $E_G^{\text{dw, eigen}}(0.01)$ is the spin down band gap from eigenvalues with occupancy below 0.01. Hence eigenvalues with occupancy above/below this criteria, which we denote as defect states, are not considered. Following we will list the occupancy parameter as a single value, such that $occ = 0.1$ represent occupancy equal to 1- 0.1 and 0 + 0.1. Applying this to SQS D we get the results listed below in table 7.3, note that $E_G^{\text{up, eigen}}$ is constant from the fact that only the spin down states contain defects.

occ	$E_G^{\text{up, eigen}}$ (meV)	$E_G^{\text{dw, eigen}}$ (meV)	$E_G^{\text{tot, eigen}}$ (meV)
0.5	339	0	0
0.05	339	21.0	21.0
0.01	339	49.6	49.6
0.001	339	73.3	73.3
<0.0001	339	85.7	85.7

Table 7.3: Band gap of SQS D as a function of occupancy in the eigenvalues.

Here we find that by introducing a stronger criteria on the eigenvalues, that the band gap firstly become finite at $occ = 0.05$ and converge to 0.085 eV by "removing" all defect states. This happens because if we neglect certain partially filled states in the conduction band, the lowest energy eigenstate in this band increase in energy and thus minimum distance between the conduction band and valence band increase, and likewise in the valence band. Comparing to the density of states band gap plotted in figure 7.1, it's apparent that E_G^{dos} correspond to $E_G^{\text{eigen}}(0.5)$.

7.2.2 Local and projected density of states
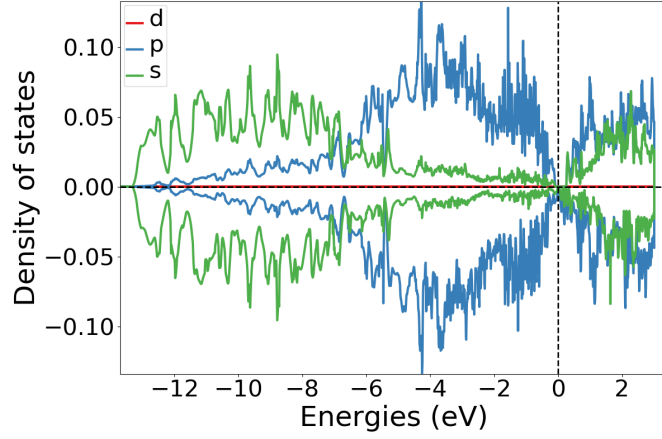
Figure 7.4: Local density of states of Si (SQS D)
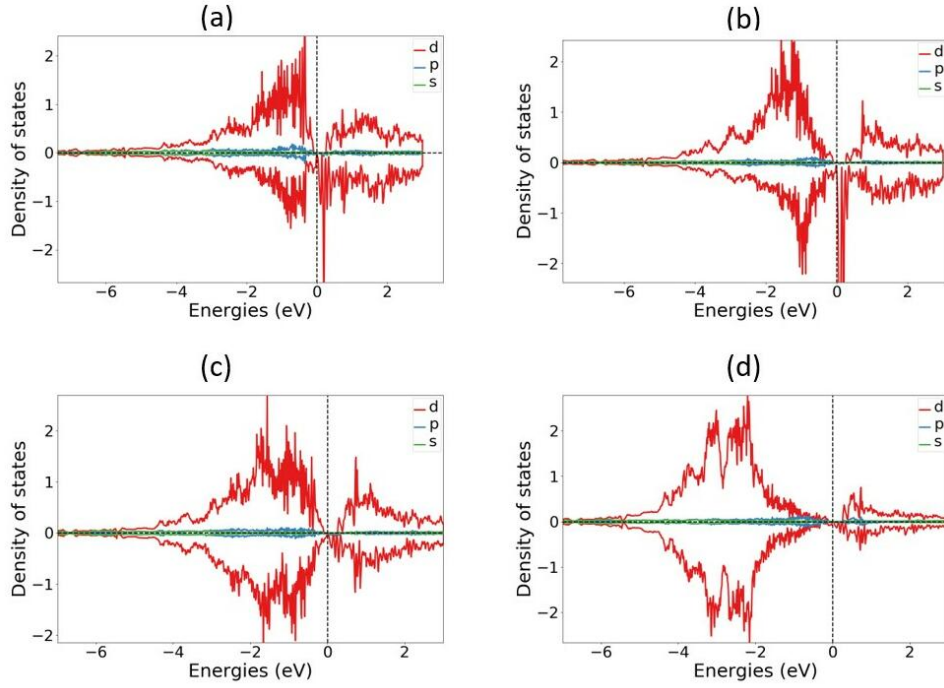
Figure 7.5: Local density of states of (a) Cr, (b) Mn, (c) Fe, (d) Ni in SQS D.

In the local density of states plotted in figure 7.3 we see that the s-electrons in Si occupy states in the lower energy regions and p electrons at slightly elevated energies closer to the Fermi energy, above E_F states are occupied by both s and p electrons almost equally. Further, the local density of states of the transition metals chromium, manganese, iron and nickel in SQS D is displayed bellow in figure 7.4. In spin down, manganese is most dominant especially above E_F, but also bellow E_F. Likewise chromium show a strong

45

presence above the Fermi energy in spin down. Both iron an Nicel show largest contribution at energies further from the Fermi energy, most notably bellow E_F. In the spin up channel we see a similar trend where chromium lie closest to E_F followed by manganese then iron and lastly nickel at the lowest energies. Another interesting observation is that the the LDOS of iron and nickel is much more symmetric between spins, than Cr and Mn. Comparing to the LDOS of iron and silicon in bulk $\beta-$ FeSi$_2$ [4] we find good agreement for both Fe and Si in this alloy .
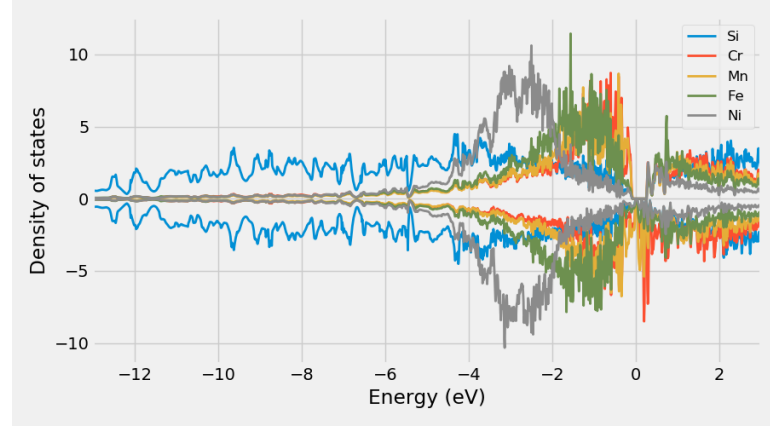
Figure 7.6: Projected density of states SQS D CFMN (fesi2) from PBE calculation

Moreover the relative positions and interplay between 3d elements and silicon as shown in the projected density of states (figure 7.5) is in good agreement with observed trends in simpler Si-rich transition metal silicides [5]. The electronic structure tends to be dominated by TM d electrons, and the valence band density of states are filled by non-bonding d states near E_F. The p-d hybridization between Si and TM elements typically fall about 6 eV bellow E_F and Si s states about 10 eV bellow. In our case we find that the Si states are pushed up closer to the fermi energy by random alloying of various 3d elements.

(a) SQS D

(b) SQS B
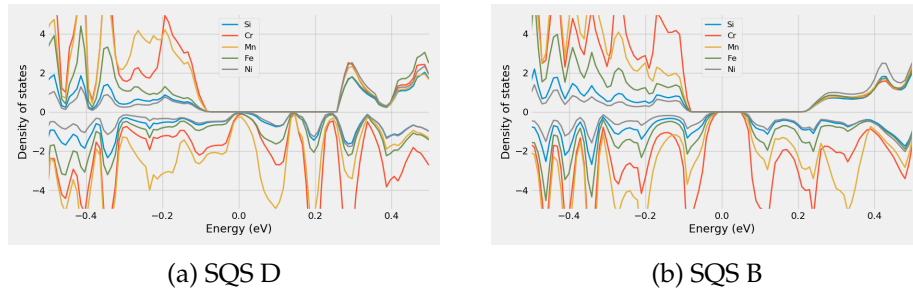
Figure 7.7: Projected density of states of SQS D and B around E_F

Above we have included the PDOS of SQS D and B but focused around E_F, from these figures we find that the spin down channel in D contain a more dominant presence of manganese especially, and some chromium as

46

compared to the semiconducting SQS B.

7.2.3 The band gap with SCAN and HSE06

As expressed previously in this work we invoke 3 level of depths GGA (PBE), meta-GGA (SCAN) and hybrid functional (HSE06) to determine the band gap of the SQSs, these results are showcased in table 7.4. Note that we do not specify eigen/dos or the occupancy here, because par SQS D the eigenvalues does not contain defect states, hence $E_G^{\text{eigen}}(0.5) = E_G^{\text{dos}}$.

SQS	XC-functional	E_G^{up} (eV)	E_G^{dw} (eV)	E_G^{tot} (eV)
A	PBE	0.0815	0.0521	0.0281
	SCAN	0	0	0
	HSE06	0.7084	0.0261	0.0261
B	PBE	0.2932	0.0523	0.0523
	SCAN	0.1470	0.0890	0.0890
	HSE06	0.2855	0.1819	0.1819
C	PBE	0.2355	0.0343	0.0343
	SCAN	0.0690	0.1124	0.1124
	HSE06	0.1744	0.0328	0.0196
D	PBE	0.3386	0	0
	SCAN	0	0.1086	0
	HSE06	0.3780	0	0
E	PBE	0.3078	0.0495	0.0495
	SCAN	0.1540	0.1112	0.1048
	HSE06	0.5476	0.0133	0.0133

Table 7.4: Band gap calculated with PBE, SCAN and HSE06 XC-functionals of (CrFeMnNi)Si$_2$ SQSs.

We will begin dissecting table 7.4 by comparing SCAN to PBE. The first distinction we make notice of is in SQS A. In this supercell calculations with the SCAN functional predicts a metalic compound, contrary to the the PBE band gap of 0.03 eV. Alike the band gap of SQS D discussed previously, the 0 band gap in this structure with SCAN is caused by defect states. Neglecting such states and evaluating the band gap from just completely filled and empty eigenstates yield $E_{G,\text{SCAN}}^{up,eigen}(0.99, 0.01) = 0.0316$ eV and $E_{G,\text{SCAN}}^{dw,eigen}(0.99, 0.01) = 0.0531$ eV, and a resulting semiconductor with a band gao of 0.0316 eV. This value seems to agree better with the PBE band gap of this supercell, but we observe that E_G^{up} is larger in PBE. This is a recurrent patter with SCAN across all five SQSs, where $E_{G,\text{SCAN}}^{\text{up}} < E_{G,\text{PBE}}^{\text{up}}$, and moreover $E_{G,\text{SCAN}}^{\text{dw}} > E_{G,\text{PBE}}^{\text{dw}}$. This can be seen in figure 7.7, where we plot the density of states of SQS E (a, b) and C (c, d). Note that the SCAN

band gap in C have the opposite spin polarization compared to PBE, this is also the case in SQS D.

(a) SQS E PBE

(b) SQS E SCAN

(c) SQS C PBE

(d) SQS C SCAN
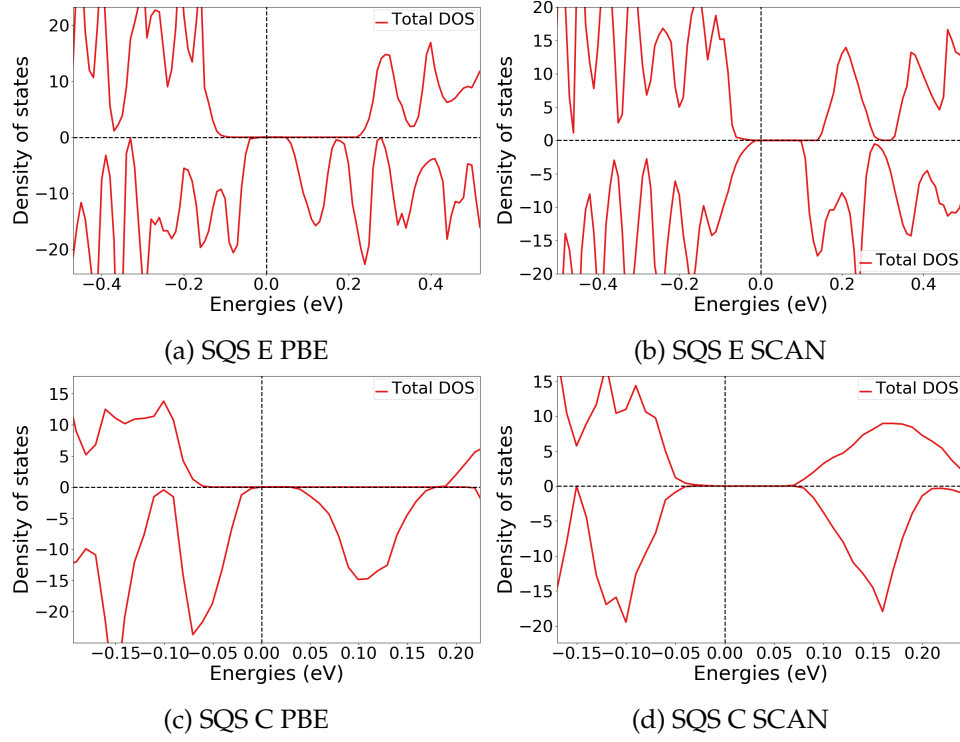
Figure 7.8: Density of states illustrating the band gaps from PBE and SCAN calculations for SQS E and D.
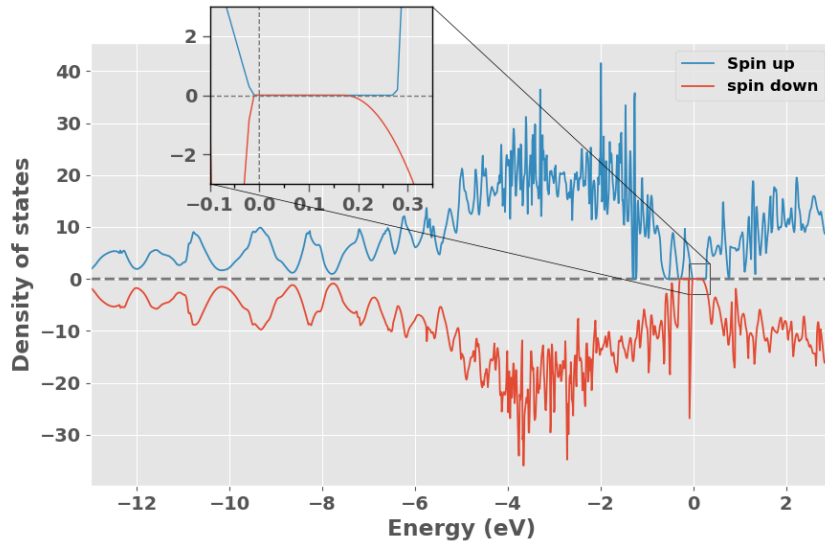
Figure 7.9: Density of states of SQS B with HSE06

With the HSE06 functional we observe the opposite trend in SQS A and E, where $E_{G,\,HSE06}^{up} > E_{G,\,PBE}^{up}$ and $E_{G,\,HSE06}^{dw} < E_{G,\,PBE}^{dw}$. But in other cases

$E_{G, \text{HSE06}}^{\text{up}}$ is lesser (SQS C) or similar to PBE (SQS B and D). On the other hand $E_{G, \text{HSE06}}^{\text{dw}}$ is consistently smaller in all structures compared to PBE, with the exception of SQS B. In this structure the HSE06 functional predicts large band gaps in both spins, as seen from the density of states plotted in figure 7.8.

As we covered in section 5.1, the hybrid functional is much more computationally demanding compared to SCAN and PBE. To reduce the cost of the HSE06 functional we performed such calculations in this project with a lower density of k-points, see section 6.1. The narrow mesh of k-points is an important factor to mention in relation to the HSE06 band gaps, that could lead to artificially exaggerated band gaps as the low density of k-points could fail to encapsulate the exact minimum transition between the valence band and conduction band.

XC-functional	Transition (k-point)
PBE	$(0.250,0.000,0.250) \rightarrow (0.000,0.000,0.000)$
SCAN	$(0.250,0.000,0.250) \rightarrow (0.000,0.333,0.000)$
HSE06	$(0.500,0.000,0.000) \rightarrow (0.000,0.000,0.000)$

Table 7.5: Minimum gap between k-point in valence band and conduction band in SQS B from PBE, SCAN and HSE06

From table 7.5, we observe that all 3 functionals find different band gaps, a concerning factor is that the highest energy k-point in the valence band from PBE calculations (0.250, 0.000, 0.250) is not considered in the HSE06 calculation with the narrow grid of 2x2x2 k-points. Thus one may suspect that the HSE06 calculation overlook the minimum transition and hence return an enlarged band gap. This could for instance be the case in $E_{G, \text{A}}^{up}$ and $E_{G, \text{B}}^{dw}$ where HSE06 predicts much larger values compared to PBE. However without an experimental baseline of the structure, we can not conclude that this is the case. As in the other SQSs we find examples where HSE06 produce similar or lower values than PBE despite of the smaller number of k-points. The concept of sufficient k-points is especially an important matter in metallic systems, as these are known to require a more dense mesh of points to accurately map the Fermi-surface [6]. However, further investigation of the importance of k-points was not possible within the time-frame of this project.

As stated in section 6.2, we did not manage to converge hybrid calculations with the tetrahedron method, and overcame this problem by first calculating the charge density with Gaussian smearing and utilize the density to expedite calculation with TBC. The respective band gaps from these methods are displayed in table 7.6 for the five SQSs of the (CrFeMnNi)Si$_2$ system. Here we calculate the band gap from the eigenvalues at different cutoff occupancy *occ* to highlight the part of defect states. Calculations with Gaussian smearing was tested with smearing width *sigma* equal to 0.05 eV and 0.005 eV.

SQS	Smearing (type) width (eV)	$E_G^{up,eigen}(0.5)$ (eV)	$E_G^{dw,eigen}(0.5)$ (eV)	$E_G^{up,eigen}(0.99)$ (eV)	$E_G^{dw,eigen}(0.01)$ (eV)	$E_G^{tot,eigen}(0.5)$ (eV)	$E_G^{tot,eigen}(0.99,0.01)$ (eV)
A	Gaussian (0.05)	0.7837	0.1493	-	0.2984	0.1493	0.2984
	Gaussian (0.005)	0.2117	0.1013	-	-	0.1013	-
	TBC	0.7084	0.0261	-	-	0.0261	-
B	Gaussian (0.05)	0.2783	0.1702	0.2988	0.3136	0.1506	0.2979
	Gaussian (0.005)	0.2838	0.1823	-	-	0.1801	-
	TBC	0.2855	0.1819	-	-	0.1807	-
C	Gaussian (0.05)	0.1078	0.1066	0.2405	0.1839	0.0650	0.1839
	Gaussian (0.005)	0.1304	0.0222	-	-	0.0222	-
	TBC	0.1744	0.0328	-	-	0.0196	-
D	Gaussian (0.05)	0.3661	0.0592	-	0.1872	0.0592	0.1872
	Gaussian (0.005)	ND	ND	ND	ND	ND	ND
	TBC	0.3780	0	-	0.2665	0	0.2637
E	Gaussian (0.05)	0.6653	0.1439	-	0.1675	0.1439	0.1675
	Gaussian (0.005)	0.5825	0.1211	-	-	0.1211	-
	TBC	0.5476	0.0133	-	-	0.0133	-

Table 7.6: Band gap from HSE06 calculations with gaussian smearing and smearing width $sigma$ equal to 0.05 and 0.005, and the tetrahedron method (TBC). "-" mean unchanged values, "ND" means not done.

From table 7.6 we observe that the case of defect states is only a concern at larger smearing widths with Gaussian smearing. Contrary to previous cases, we find here finite band gaps despite of defect states. By comparing E_G^{up} and E_G^{dw} at $occ = 0.5$ and $occ = 0.01$, the defects appear to have a lesser role in spin up, as par SQS C the band gap in spin up is either consistent or only marginally different between the defect band gap and the hypothetical defect less band gap. E_G^{dw} on the other hand increase significantly by removing the defect states. The Gaussian smearing method is generally in better agreement with TBC at lower smearing width. But even in this case we find several dissimilarities. In A and E E_G^{dw} is larger with the Gaussian method, additionally E_G^{up} is much lower in A. In this project we have based our choice of numerical smearing on the advice on the VASP manual that state that for accurate total energies and density of states in semiconductors one should opt for the tetrahedron method [7]. However since our system is comprised of metals we include the results from utilizing Gaussian smearing as well. There are of course many more factors that affect the accuracy and reliability of both methods, but these are outside the scope of this project.

The fact that all 3 functionals and five SQS in majority agree on the presence of a band gap is in itself an overwhelmingly positive result that allow us to state with high certainty that the potential high-entropy silicide $(CrFeMnNi)Si_2$ is in fact a semiconductor or possibly a half-metal based on the observed spin polarization and the utmost stable SQS. Regarding the 3 functionals applied in this project, we experience best cohesion between PBE and HSE06 that both agree on a spin up polarization of the band gap, while SCAN predicts more symmetric band gaps. This can also be seen from the magnetic moment, with PBE and HSE06 the final magnetic moment (per atom) is 0.083 μ_B across all SQSs, with SCAN this is reduced to half as much. This result could be related to the known drawbacks of SCAN and magnetic materials. In the nonmagnetic $\beta-$ FeSi$_2$ structure we find better agreement between PBE and SCAN. Both correctly predict that the material is nonmagnetic, however compared to the experimental value of about 0.85 eV and the PBE band gap of 0.65 eV, we get a smaller band gap of 0.61 eV with SCAN. Thus the SCAN functional does not necessarily result in increased accuracy over PBE even in the nonmagnetic material. To conclude this section on the band gap $(CrFeMnNi)Si_2$, when studying the band gap with DFT, particularly PBE is well known to underestimate the band gap of the real material as in FeSi$_2$. Therefore a band gap found with PBE would with high probability be replicated/increased in the real material.

7.2.4 Pair distribution functions

The probability distribution functions of SQS D and E can be seen bellow in figure 7.10, the PDFs corresponding to the remaining SQSs can be found in appendix .. . We include the PDFs of SQS D and B because as stated D is the most stable atomic configuration and hence the most representative of a potential real compound, and B to investigate distinctions between the half-metallic structure D and the semiconducting B which with HSE06 yielded substantial band gaps in both spins, recalling also that this is just very slightly bellow D in terms of stability. In the analysis we will put special emphasis on the nearest neighbor interactions since these are the most crucial in deciding the functional properties of a material.
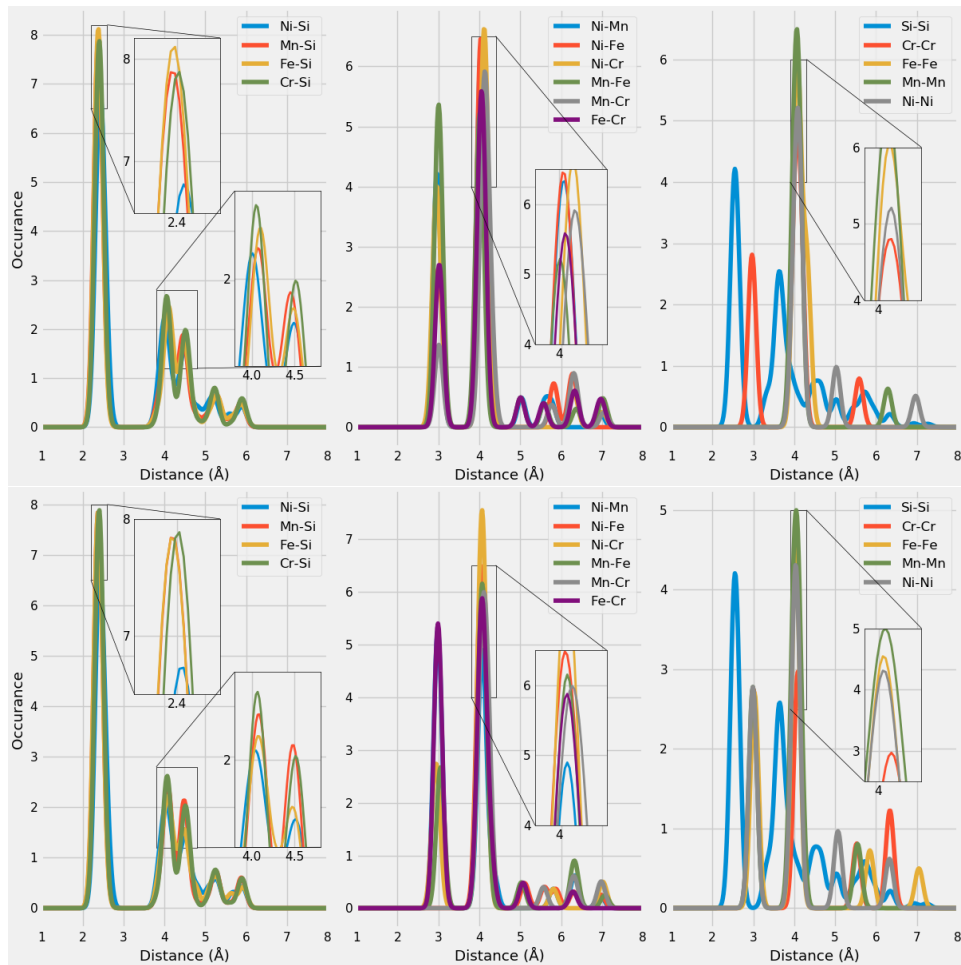
Figure 7.10: Probability distribution function of SQS D (top) and B (bottom)

We see that the relative positions of the PDFs remain consistent though both SQSs. With the aid of the ICSD (insert citation), we can compare the figure .. to the expected PDFs based on a number of experiments from a host of different compounds. As our compound contain a total of 15 different bonds, comparing each one to the ICSD values would be an exhaustive process. For our purpose we are satisfied by comparing the 4

different metal-Si bonds. We find that the preferred bond-length of TM-Si is observed at two values, the most dominant being the shorter of the two. For Fe-Si these are between 2.25-2.75 and 4-5, Mn-Si 2.25-2.75 and 3.5-5. Ni-Si lie between 2.25-2.5 and 3.85-5 and Cr-Si between 2.35-2.65 and 4-5.Clearly, the PDFs of the alloys are in good agreement with the listed values for Tm-Si bonds, with the most occurring bond length falling at around 2.4 Å for all TMs, and lesser occurrence between 4.0 - 4.5 Å. The height of the respective peaks is somewhat consistent in both structures, other than slightly reduced Fe-Si occurrence at 2.4 Å in B.

In contrast to the TM-Si bonds, we observe several distinctions between metal bonds in SQS D and B. Covering all would be tedious and not to insightful, instead we emphasize the bonds of Mn and Cr as this is where we found the biggest discrepancy in the PDOS. From the different TM-TM bonds (middle) of figure 8.8 we observe that the Mn-Fe bonds are most occurring at short distances in D and bigger distances in B, meaning that manganese and iron atoms are placed further from each other in structure D. **correct?** Similarly the bonds between Cr and Fe indicate that these atoms lie closer in B than D. In contrast the nickel and manganese/chromium bonds point to a closer distance in B for Ni-Mn and Ni-Cr in D, and a greater distance between Ni and Mn in D and Ni and Cr in B. **Litt kronglete kanskje?** In terms of the homogeneous bonds, the properties of both Cr-Cr bonds and Mn-Mn bonds are more or less alike in both structures besides some majority at shorter distance in D (The red Cr-Cr line at 3Å is underneath the grey Ni-Ni line in B in figure 8.8 (bottom right)). A more significant distinction is that both Ni-Ni and Fe-Fe bonds are found at 3 Å and 4 Å in B, but exclusively 4 Å in D.

Both the Fe-Fe and Ni-Ni bonds are in better agreement with the ICSD histograms, as the most occurring distance for these bonds are between 4-4.9 Å and additionally around 2.5 Å. **More comparisons to ICSD, ask O.M**. As a conclusion on the PDFs of this compound, we locate a pattern where the Si-Si bonds are identical and only very minor differences between TM-Si bonds in SQS D and B. This is a result of how the structures are generated with the SQS method. In th FeSi2 structure the silicon atoms are placed as before in the new supercells, but the TM elements are "randomly" distributed. Thus, it's reasonable that also here we would find the major differences between SQSs in the PDFs.

7.2.5 SQS size

Above we have presented the results of a high-entropy silicide (CrFeM-nNi)Si$_2$ investigated by 5 48 atom SQSs with a volume of 700Å^3. This intermediate size allowed for the use of more complex XC-functionals, and secondly enabled a broad study of distinct permutations and compositions as we will discover in the next chapters. However the application of the special quasi-random structures method to HEAs is not necessarily straightforward. Recalling from section 4.3 the first initial concern is the size of the SQS model and if it's sufficient enough to correctly model the disordered multi-component structure. In this section we will consider this problem by studying the difference between the 48 atom SQS to that of a 96 and 192 atom SQS with volume 1200Å^3 and 2400 Å^3 respectively. The computational demand for the 3 sizes is seen below in figure 7.11 where we plot the number of CPU hours as a function of number of atoms, which yield roughly a N^3 dependence.
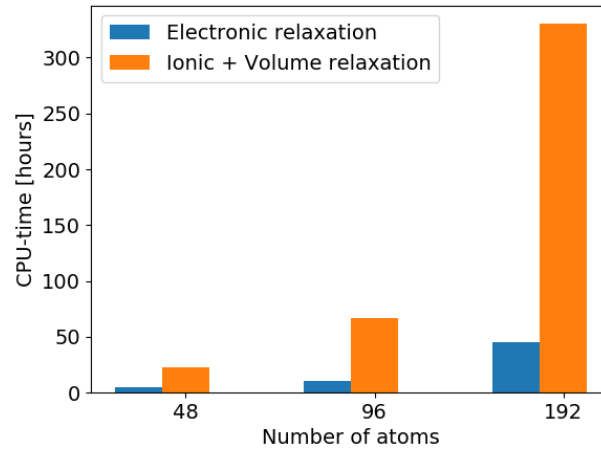
Figure 7.11: CPU time, **Make log plot instead**

Bellow we list the mean and standard deviation of the total energy, magnetic moment and enthalpy of formation of the 3 sizes in table 7.6, and band gaps in table 7.7.

SQS size	Toten (eV)		Mag (μ_B)		ΔH (eV)
	mean	std	mean	std	mean
48 atoms	- 6.6105	..	0.0833	0.0000	-11.5000
96 atoms	- 6.6092	0.0021	0.0708	0.0114	- 22.8752
192 atoms	- 6.6123	0.0022	0.0761	0.0171	- 46.6654

Table 7.7: Overivew 48, 96 and 192 SQSs.

As seen from table 7.4 both the total energy and magnetism remain more or less consistent throughout all sizes, this is a good indication of that the 48 atom model can adequately model the alloy. **Something on the formation enthalpy.** The band gap as seen in table 7.7 is first of all evident across all 3 SQS models and show similar polarization favoring the spin up direction. In several cases, we find that the magnitude of the band gap lessen with increasing SQS size.

SQS size	SQS	$E_G^{up,eigen}(0.5)$ (eV)	$E_G^{dw,eigen}(0.5)$ (eV)	$E_G^{tot,eigen}(0.5)$ (eV)
48 atoms	A	0.0815	0.0521	0.0281
	B	0.2932	0.0523	0.0523
	C	0.2355	0.0343	0.0343
	D	0.3386	0	0
	E	0.3078	0.0495	0.0495
96 atoms	**A**	0.1705	0.0442	0.0367
	B	0.1386	0.0270	0.0270
	C	0.1347	0.0363	0.0075
	D	0.0892	0.0398	0.0398
	E	0.1610	0	0
192 atoms	A	0.1197	0.0321	0.0321
	B	0.1444	0	0
	C	0.1867	0	0
	D	*0.0478*	*0.0339*	*0*
	E	*0.0131*	*0.0184*	*0.0131*

Table 7.8: Band gap of SQSs of 48, 96 and 192 atoms each of (CrFeMnNi)Si$_2$. The names are arbitrary, ie A in 48 does not equal A in 96 or 192.

Similar to structure D in the 48 atom SQS we find that the 0 value in SQS E in the 48 atom model suffers from defect states and find $E_G^{dw,eigen}(0.90, 0.10) = 0.016$ eV. The same is true for SQS B and C (192), but require $occ = 0.999, 0.001$ to locate a small nonzero spin down band gap. The band gap in SQS D and E (192) on the other hand is finite at $occ = 0.5$ but can be enlarged from increasing occ. In D we get $E_G^{up,eigen}(0.99) = 0.075$ eV and $E_G^{dw,eigen}(0.01) = 0.05$ eV and similarly $E_G^{up,eigen}(0.99) = 0.05$ eV, and $E_G^{dw,eigen}(0.01) = 0.048$ eV in E. In such cases where the eigenvalues inclusive of defect states return a finite band gap, the density of states does not. This is seen in figure .. for SQS E (192).

Drawing any conclusion on the band gaps is difficult seeing as we find very different results within the all 3 sizes. Based solely on the most stable SQS it's clear that the larger cell produce a much lower and different band gaps compared to the moderate SQS sizes which are much more similar. However also here we find that the gap in the 96 cell is only abort half of the 48 atom cell. However as seen in table 7.7 we also find evidence of large
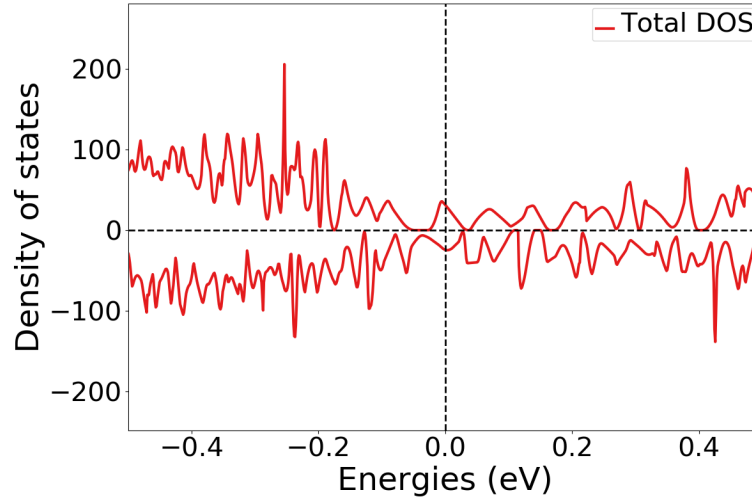
Figure 7.12: Density of states of SQS E 192 atom SQS.

band gaps in the larger cells in other atomic configurations. This goes back to section .. when we mentioned that one of the biggest drawbacks of the special quasi-random structures method is the large number of possible atomic configurations, thus in order to conclude between results in this project the most sensible point is to consider the most stable SQS, but as seen from the very varying properties between SQSs of the same model, this does not necaccarly been the most stable SQS if we trialed 20 SQSs instead of just 5. An additional point is the magnetic property, here we only applied one configuration to base the stabiliy on, thus it's very probable that fine tuning the magnetic moments could result in different properties.

Looking at the pair distribution functions in figure 7.11 we see that the local ordering and short-range interactions is well represented and identical across all three sizes. The distinctions of preferences could as stated above simply be a product of the uniqueness of the SQSs more so than the size. On the other hand the larger SQSs clearly provide a better description of large-range interactions, that is not nearly as present in the smaller cell. However as seen in table 7.4 and in accordance with the fundamental concept of the special quasi-random structures method is that the functional properties is mostly determined by short-range effects in the lattice. Therefore, even though the bigger SQSs is a more accurate model the improvement is not justified from the cost, as illustrated in figure 7.12. And the apparent larger concern from appling the SQS method in this project is the uniqueness of each SQS.
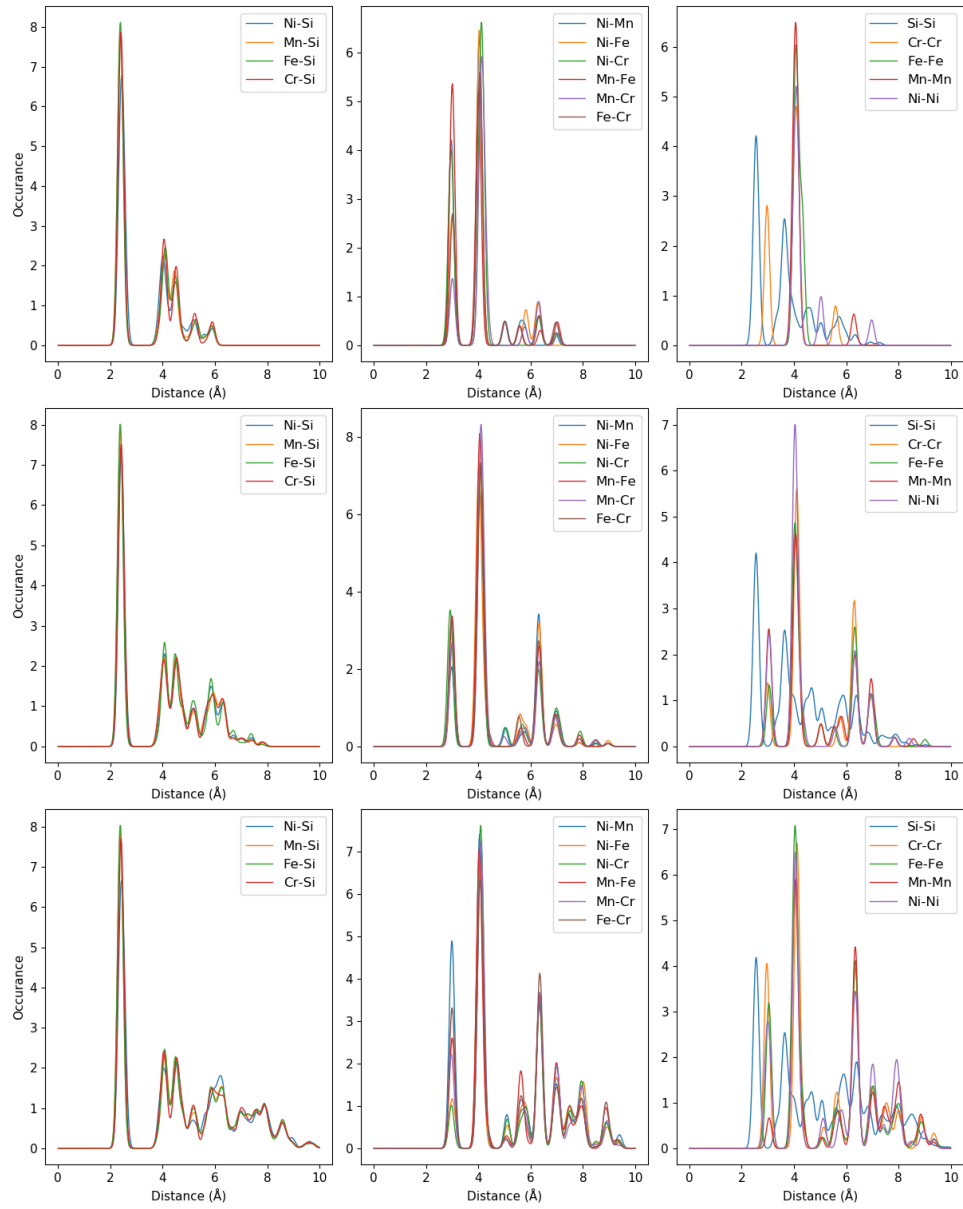
Figure 7.13: Pair distribution functions of SQS sizes (top) 48 atoms, (middle) 96 atoms, (bottom) 192 atoms

Chapter 8

Different compositions

Up until this point we have looked in detail at the high-entropy silicide $(CrFeMnNi)Si_2$ and associated SQSs. However these structures are just the center of a larger quasi-ternary phase diagram consisting of the different possible distributions of elements Thus there exists many other compositions of this particular high-entropy silicide.

8.1 Exploring the quaternary phasidiagram

In this section, we aim to expand our search of this diagram by generating SQSs of the 48 atom model slightly away from equimolar distribution of 3d elements. In table (bellow) we list the mean total energy and magnetic moment per atom with standard deviation and the enthalpy of formation of 4 compositions of the $(CrFeMnNi)Si_2$ alloy. Ideally they would differ only by one element, but the TDEP implementation insist in also reducing Nickel to stay consistent with the 48 atom supercell.

Composition	Toten (eV)		Mag (μ_B)		ΔH (eV)
	mean	std	mean	std	mean
$Cr_3Fe_3Mn_7Ni_3Si_{32}$	- 6.6947	0.0040	0.1375	0.0186	-11.9586
$Cr_5Fe_5Mn_3Ni_3Si_{32}$	- 6.6705	0.0030	0.1127	0.0223	-11.1991
$Cr_5Fe_3Mn_5Ni_3Si_{32}$	- 6.6852	0.0041	0.1375	0.0456	-10.5200
$Cr_3Fe_5Mn_5Ni_3Si_{32}$	- 6.6801	0.0036	0.0937	0.0209	-12.6426
$Cr_3Fe_3Mn_3Ni_7Si_{32}$	- 6.3921	0.0078	0.0159	0.0101	-10.9614

Table 8.1: Summary composition diagram

The first result of table .. we make notice of is that the stability, as evaluated by the enthalpy of formation can be increased beyond the eqvimolar composition. This is accomplished in two distinct permutations, one with increments to manganese relative to the other TM, and the other by reduction of chromium. Compared to the equimolar system, the magnetic moment of these compositions show a greater variation between

SQSs, as indicated by the standard deviation. Typically the most stable SQS lie around the mean value of the set. The large magnetic moment of the manganese rich permutation and the low magnetic moment in the chromium poor permutation is very much in line with the observations made in the previous section. Recalling that in the magnetic moment in the equimolar composition was largely attributed to manganese and chromium atoms in the lattice. Thus increments to manganese or reduction of chromium would following impact the magnetic moment as seen. Following the composition $Cr_5Fe_3Mn_5Ni_3Si_{32}$ where the nonmagnetic elements are reduced and the magnetic elements are increased, the final magnetic moment is among the highest of the bunch equally magnetic.

In table 8.2 we list the respective band gaps of the different compositions calculated with the PBE functional. Only the GGA functional was applied in this case because the motivation is primarily to compare the results to the parent equimolar composition and thus including 3 times as many results to calculate and analyze unnecessarily complicate the process. Thus we base this comparison between the PBE results of the new compositions to the PBE band gaps of the equimolar compound. In these compositions we find strong indication of a half-metal with less frequent SQSs with a band gap in the spin down channel than the equimolar compound. In the spin up channel on the other hand several compositions show very similar values to the equimolar composition. Between the different compositions particularly those rich in manganese provide very encouraging results and compositions poor in Mn less so. In terms of the stability we a very encouraging results of both the $Cr_3Fe_3Mn_7Ni_3Si_{32}$ and $Cr_3Fe_5Mn_5Ni_3Si_{32}$ compositions, where the most promising properties is attributed to the utmost stable configurations. in $Cr_3Fe_5Mn_5Ni_3Si_{32}$ the most stable SQS (D) is a semiconductor with a band gap around 0.1 eV.

Below in figure 8.1 we plot the projected density of states around E_F of the fist four compositions of table 8.2. Note that away from the Fermi energy the projected density of states is analogous to the parent equimolar composition. The below figures is based on the most stable SQS in each permutation, as will the analysis. Hence the features of these figures can be subject to the uniqueness of that particular SQS rather than a distinct feature of the exact composition, but as stated previously the most stable configuration provide the most likely properties of the composition within the scope of this project.

Composition	SQS	$E_G^{\text{up, eigen}}(0.5)$ (eV)	$E_G^{\text{dw, eigen}}(0.5)$ (eV)	$E_G^{\text{tot, eigen}}(0.5, 0.5)$ (eV)
$Cr_3Fe_3Mn_7Ni_3Si_{32}$	A	0.3390	0	0
	B	0.4745	0	0
	C	0.1342	0	0
	D	0.1950	0.0063	0.0063
	E	0.4211	0	0
$Cr_5Fe_5Mn_3Ni_3Si_{32}$	A	*0.003*	0	0
	C	*0.21*	0	0
	D	0.0674	0.0413	0.0372
	E	*0.362*	0	0
$Cr_5Fe_3Mn_5Ni_3Si_{32}$	**A**	0.2082	0	0
	B	0.4053	0	0
	C	0.4659	0	0
	D	0.0843	0.0121	0.0121
	E	0.3008	0	0
$Cr_3Fe_5Mn_5Ni_3Si_{32}$	A	0.3922	0	0
	C	0.1285	0	0
	D	0.2595	0.1004	0.1004
	E	0.3591	0.1003	0.0848
Cr3Fe3Mn3Ni7Si32	A	0	0	0
	B	0	0	0
	C	0	0	0
	D	0	0	0
	E	*0.04*	0	0

Table 8.2: Band gaps of various compositions of $(CrFeMnNi)Si_2$. Most stable SQS of a set is highlighted in bold text, defect band gap are listed in cursive. Some SQSs were excluded from the table due to unsuccessful calculations.
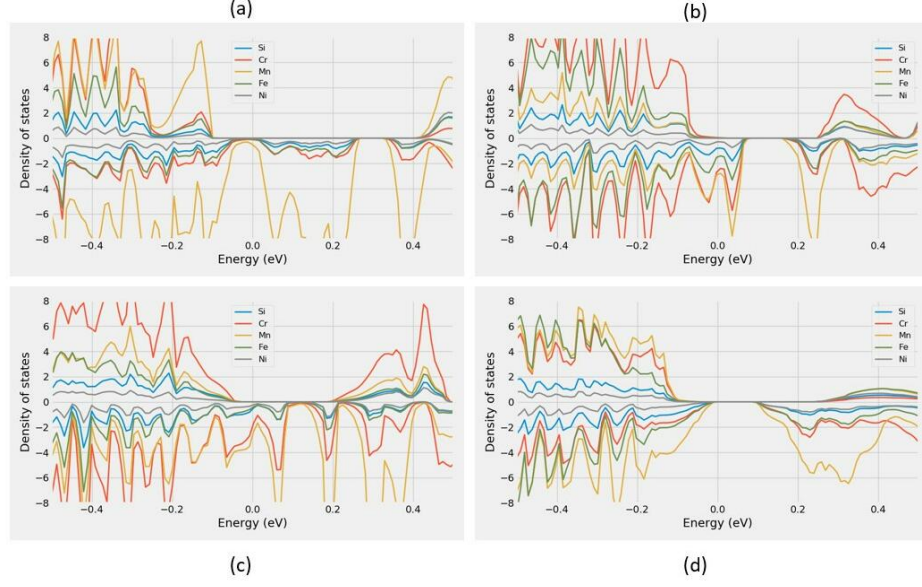
Figure 8.1: Projected density of states of (a) $Cr_3Fe_3Mn_7Ni_3Si_{32}$ (SQS B), (b) $Cr_5Fe_5Mn_3Ni_3Si_{32}$ (SQS C), (c) $Cr_5Fe_3Mn_5Ni_3Si_{32}$ (SQS A), (d) $Cr_3Fe_5Mn_5Ni_3Si_{32}$ (SQS D)

With that said, the plotted PDOSs in figure 7.1 is in good agreement with the listed values in table 7.2. $Cr_3Fe_3Mn_7Ni_3Si_{32}$ (7.1 a) and $Cr_5Fe_3Mn_5Ni_3Si_{32}$ (7.1 c) both indicate a sizable spin up band gap, further figure (7.1 d) point to a total band gap around 0.1 eV for SQS D of $Cr_3Fe_5Mn_5Ni_3Si_{32}$. On the other hand we find dissimilarity between the density of $Cr_5Fe_5Mn_3Ni_3Si_{32}$ SQS C and the eigenvalue band gap listed in table 7.2. In figure 7.1 d we find a range of forbidden energies slightly above the Fermi energy, and very small values in spin up at the Fermi energy. Similar to what we experienced in the 192 atom SQS in section 7.4, the eigenvalues report a finite band despite of defect states. Therefore the density of states is not completely zero at E_F.
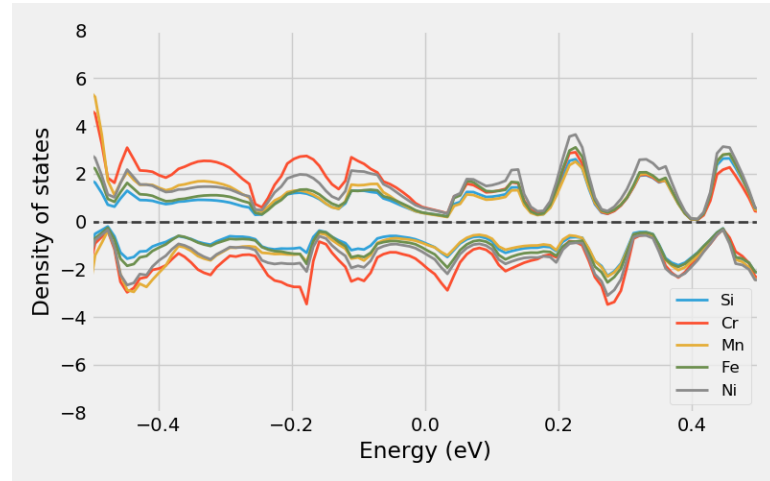
Figure 8.2: Projected density of states of $Cr_3Fe_3Mn_3Ni_7Si_{32}$ around E_F

In figure 8.6 we saw that electrons from manganese atoms in particular was a key contributor as to why the spin down channel of $(CrFeMnNi)Si_2$ was metallic in the stable supercell D. This is also largely the case in the permutations shown above in figure 8.12. The proportion of manganese atoms in the alloy seems to offer a very positive effect on the band gap in spin up, but is often detrimental to spin down. This is seen in figure 8.12 (a) and (c) for $Cr_3Fe_3Mn_7Ni_3Si_{32}$ and $Cr_5Fe_3Mn_5Ni_3Si_{32}$ respectively, that both contain increased amounts of manganese. By reducing the number of Mn as in (b) we still find that the Mn electrons plague the states at E_F in spin down. In analog we see from (b) and (c) that also Cr negatively impacts to the band gap especially in spin up. The sole permutation with clear evidence of a spin down gap is from the chromium poor permutation plotted in (d). Also in this structure we see that the effects of Mn around E_F is dampened in comparison to the other permutations, despite containing relatively increased amounts of Mn to the eqvimolar alloy.

An important property of these results is that because each permutation alters simultaneous elements, interpreting and relating the results to a particular alteration is challenging. For example, is the result of the $Cr_5Fe_3Mn_5Ni_3Si_{32}$ permutation a consequence of less Fe or increments to both Cr and Mn? Furthermore is the large band gap in spin up of $Cr_3Fe_3Mn_7Ni_3Si_{32}$ a product of increasing manganese or reducing the other elements. From the comparatively large gaps in spin up of $Cr_3Fe_3Mn_7Ni_3Si_{32}$ and $Cr_3Fe_5Mn_5Ni_3Si_{32}$ and the more present Cr states in spin up in the Cr rich permutations we here conclude that the band gap is related to lessening of chromium, more so than other effects. However we see from both $Cr_5Fe_5Mn_4Ni_3Si_{32}$ and $Cr_3Fe_3Mn_3Ni_7Si_{32}$ (figure 8.2) in addition to the manganese rich composition that Mn plays a vital role on the band gap of these structures. It's clear that the $Cr_3Fe_5Mn_5Ni_3Si_{32}$ alloy manage to strike a balance between 3d elements that results in a specific interplay and correspondingly very promising properties.

8.2 Replacing elements

In similar fashion to the previous sections, we here begin by presenting the mean and standard deviation of the total energy and magnetization of a set of SQSs corresponding to different high-entropy silicides of the $Fesi_2$ unit cell. The compositions we have tested are deliberate combinations intended to investigate both the impact of manganese by replacing the element with Co or Ti, and concepts related to HEA theory such as the atomic size effect. Furthermore Co is a very common element in many stable HEA, as seen in section 2.2, thus we include 3 compositions with Co to study the impact on stability and the functional properties. The results of the aforementioned alloys can be seen bellow in table 9.1, note that all compounds contain a total of 48 atoms as before.

Composition	Toten (eV)		Mag (μ_B)		ΔH (eV)
	mean	std	mean	std	mean
$Cr_4Fe_4Co_4Ni_4Si_{32}$	- 6.4655	0.0056	0.0083	0.0155	- 12.7536
$Co_4Fe_4Mn_4Ni_4Si_{32}$	- 6.4731	0.0046	0.0000	0.0000	- 15.0836
$Cr_4Fe_4Ti_4Ni_4Si_{32}$	- 6.4217	0.0087	0.0305	0.0293	- 7.5040
$Cr_4Fe_4Mn_4Ti_4Si_{32}$	-6.6994	0.0071	0.1142	0.0641	- 7.3060
$Cr_4Fe_4Mn_4Co_4Si_{32}$	-6.7687	0.0034	0.1331	0.0326	- 13.7796

Table 8.3: Overview new compositions

From table 9.1 we see that the stability of the relative compositions vary greatly. By introducing cobalt to the alloys, particularly at the cost of manganese result in a large positive effect on the stability, contrary replacing either manganese or nickel with titanium significantly lowers the stability. **Wait for new formation enthalpies.** In table 9.1 we have listed the mean magnetic moment of the compositions, in line with previous results in this project the magnetization is very dependent on chromium and manganese. This is seen by the overall lowest magnetic moments in the two compositions without these elements, and reversely the highest magnetic moments is found for compositions with both Cr and Mn. Comparing the magnetic moment of $(CrFeCoNi)Si_2$ and $(CoFeMnNi)Si_2$ it seems in our study that chromium is most responsible for the magnetic moment in these alloys. Furthermore we find that substituting Ni with both Ti and Co result in more magnetic compounds. These are truly surprising results, one would expect that the magnetic moments would be larger in the ferromagnetic elements Ni, Fe and Co than Cr, Mn and ti. This could go back to our simplistic and superficial study of the magnetic properties in this project, additionally the PBE functional as we covered in section .. have shown limitations for 3d elements and particularly Ni. Thus this could be a factor affecting our results. Another factor is that we here based our comparison on the mean values between 5 SQSs. As we have experienced throughout this project the unieqeness of the SQSs can be troublesome to

handle, and our best guess is to study the most stable super-cell. Bellow in table 9.2 we list the magnetic moments of the most stable SQSs. Here we find several dissimilarities to the mean value such as the $Cr_4Fe_4Co_4Ni_4Si_{32}$ being nonmagnetic in the most stable supercell. Thus based on the utmost stable configurations we can state that replacing either Cr or Mn (with Co) removes the magnetic moment in the alloy. Furthermore we find from these supercells that the magnetic moment is reduced by replacing Ni with Ti, and increased from Co. These results are in much better accordance with previous knowledge of ferromagnetic elements and their interplay in high-entropy alloys.

Composition	Magnetic moment (μ_B)
$Cr_4Fe_4Co_4Ni_4Si_{32}$	0
$Co_4Fe_4Mn_4Ni_4Si_{32}$	0
$Cr_4Fe_4Ti_4Ni_4Si_{32}$	0,0653
$Cr_4Fe_4Mn_4Ti_4Si_{32}$	0,0785
$Cr_4Fe_4Mn_4Co_4Si_{32}$	0,1666

Table 8.4: Final magnetic moment of the most stable supercell of each composition.

In regards to the band gap of these compositions, we find most to be metals. The band gap of the most stable SQS of each composition is listed in table 4.3, where we calculate the band gap from the eigenvalues at different occupancy cutoffs. As before the 0 band-gap is caused by defect states in the band gap. By increasing the criteria, in other words only consider states with occupancy above a certain threshold, the band gap become finite at $occ = 0.1$ and converge to around $0.02 - 0.06$ eV depending on composition, when only considering full/empty states.

Composition	occ	$E_G^{\text{up, eigen}}$ (eV)	$E_G^{\text{dw, eigen}}$ (eV)	$E_G^{\text{tot, eigen}}$ (eV)
CrFeCoNiSi$_2$	0.5	0	0	0
	0.1	0.00095	0.0399	0.00095
	0.01	0.063	0.063	0.063
CrFeTiNiSi$_2$	0.5	0.0067	0	0
	0.1	0.061	0.0087	0.0087
	0.01	0.061	0.037	0.037
CoFeMnNiSi$_2$	0.5	0	0	0
	0.1	0.0037	0.0037	0.0037
	0.01	0.0268	0.0268	0.0268
CrFeMnTiSi$_2$	0.5	0	0	0
	0.1	0.021	0.00049	0
	0.01	0.03	0.03	0.022
CrFeMnCoSi$_2$	0.5	0.461	0	0
	0.1	0.607	0.0218	0.0218
	0.01	0.607	0.0245	0.0245

Table 8.5: Band gaps of the most stable SQS of $\beta-$ FeSi$_2$ high-entropy silicide compositions as a function of occupancy in the eigenvalues.

The one exception to the metallic compositions is the CrFeMnCoSi$_2$ composition with a gap of around 0.5 eV in the spin up channel. As seen in previous cases, this structure despite of the large band gap contains also a small amount of defect states. This is seen in the projected density of states plotted in figure 4.1, where we observe small nonzero values of the density of states at the Fermi energy. The PDOSs of the other compositions is found in appendix ..
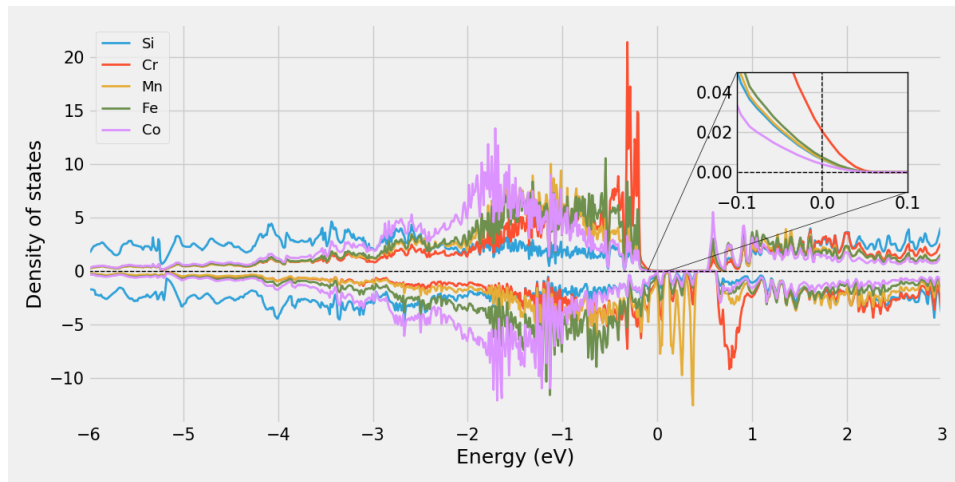

Figure 8.3: Projected density of states of (CrFeMnCo)Si$_2$.

Contrary to the above case, inserting Co in the place of manganese clearly result in a metallic structure, as seen in the density of states in figure 9.2 a. Replacing Mn with Ti instead we recall from table 9.3 a a very small defect band gap in spin up, however from figure 9.2b we observe that E_G^{dos} is equal to zero, thus $E_G^{\mathrm{dos}} \neq E_G^{eigen}$. Comparing the density of states of $(CrFeCoNi)Si_2$ and $(CrFeTiNi)Si_2$ tha the latter is magnetic and the former nonmagnetic, as we discussed previously.
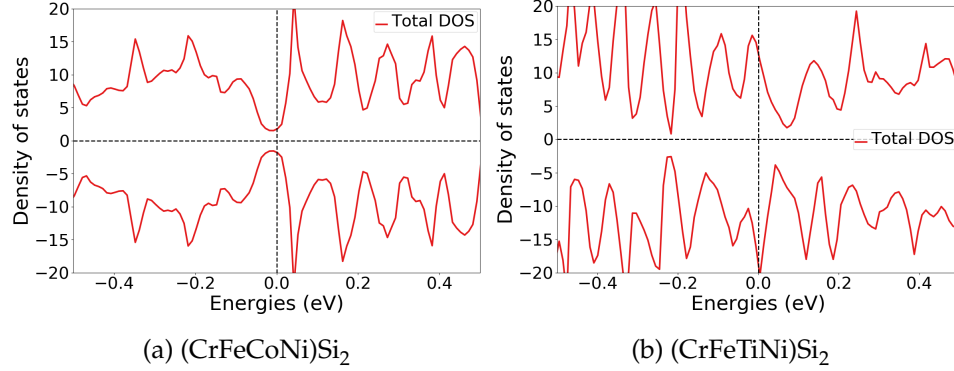

(a) $(CrFeCoNi)Si_2$

(b) $(CrFeTiNi)Si_2$

Figure 8.4: Density of states of a) $(CrFeCoNi)Si_2$ and b) $(CrFeTiNi)Si_2$.

Above we have looked at the band gap of the most stable SQS of each composition, but as we have experienced in other cases in this project, the properties can vary between SQSs of the same composition. In both $CrFeCoNiSi_2$ and $CrFeMnTiSi_2$ we found only metalic supercells with the exception of one SQS in the latter with a very small defect band gap in spin up. Similarly small defect band gaps was observed in two SQSs of $CrFeTiNiSi_2$ and the rest as metals. In $CrFeMnCoSi_2$ we found a large defect band gap in spin in the most stable configuration, here we find similar band gaps in two other SQSs as well, and two structures. The most interesting case was found in $CoFeMnNiSi_2$ where we observed small total band gaps without defect states in two SQSs, these are seen in figure 9.3. In agreement with the nonmagnetic character of this composition, the DOS is symmetric with respect to spins.
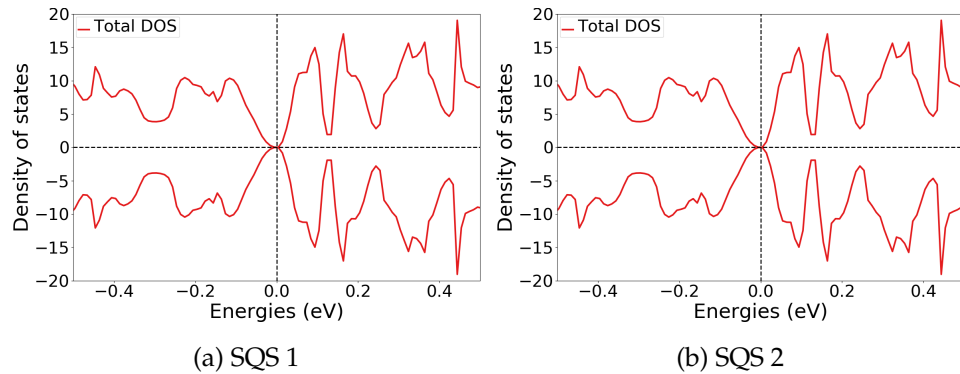

(a) SQS 1

(b) SQS 2

Figure 8.5: Density of states of two SQSs of $(CoFeMnNi)Si_2$.

Thus we find examples where the most stable SQS is representative of the set, and other cases where we observe meaningful distinctions between the most stable and other possible configurations. Because of limited time examining properties and options affecting both the magnetism and stability of the alloys and respective supercells, it's important to consider the different configurations as a a broader search would not necessarily yield the same relationship. And to show some of the limitations that apply when using the special quasi-random structures method. **Can I say this?**. It appears that we find limited success overall, but particularly when substituting either Cr or Mn as outlined in the previous section. Furthermore Ti is not as successful as Co. **Continue conclusion this and entire project**

Part IV

Conclusion

Write conclusion here

Bibliography

[1]   S. J. Clark et al. 'Structure and electronic properties of FeSi$_2$'. In: *Phys. Rev. B* 58 (16 Oct. 1998), pp. 10389–10393. DOI: 10.1103/PhysRevB.58. 10389. URL: https://link.aps.org/doi/10.1103/PhysRevB.58.10389.

[2]   J. Acker et al. 'Thermodynamic properties of iron silicides FeSi andα-FeSi2'. In: *The Journal of Chemical Thermodynamics* 31.12 (1999), pp. 1523–1536. ISSN: 0021-9614. DOI: https://doi.org/10.1006/jcht. 1999.0550. URL: https://www.sciencedirect.com/science/article/pii/ S0021961499905505.

[3]   Voicu Popescu and Alex Zunger. 'Effective Band Structure of Random Alloys'. In: *Phys. Rev. Lett.* 104 (23 June 2010), p. 236403. DOI: 10.1103/ PhysRevLett.104.236403. URL: https://link.aps.org/doi/10.1103/ PhysRevLett.104.236403.

[4]   R. Eppenga. 'Ab initio band-structure calculation of the semiconductor β-FeSi2'. In: *Journal of Applied Physics* 68.6 (1990), pp. 3027–3029. DOI: 10.1063/1.346415. eprint: https://doi.org/10.1063/1.346415. URL: https://doi.org/10.1063/1.346415.

[5]   H Lange. 'Electronic properties of semiconducting silicides'. In: *physica status solidi (b)* 201.1 (1997), pp. 3–65.

[6]   Stewart Clark. 'Modelling complex structures'. URL: http://cmt.dur.ac. uk/sjc/thesis/thesis/node28.html.

[7]   *ISMEAR - Vaspwiki*. URL: https://www.vasp.at/wiki/index.php/ISMEAR.